JET–P(99)65

T J J Tala et al

Predictive Modelling of Optimised Shear Scenarios for High Performance Experiments on JET

JET–P(99)65

Predictive Modelling of Optimised Shear Scenarios for High Performance Experiments on JET

T J J Tala[1], Yu F Baranov, J A Heikkinen[1], S J Karttunen[1], V V Parail, F X Söldner[2], A Taroni[3].

JET Joint Undertaking, Abingdon, Oxfordshire, OX14 3EA,
[1]Permanent address: Association Euratom-Tekes, VTT Energy, P O Box 1604, FIN-02044 VTT, Finland.
[2]Present address: European Commission, Directorate-General Energy, Bruxelles, Belgium.
[3]Present address: European Commission, Directorate-General XII, Bruxelles, Belgium.

Preprint of a Paper to be submitted for publication in Nuclear Fusion

February 2000

Abstract

Modelling of lower hybrid current drive with transport calculations is performed with the JETTO transport code which has been upgraded by implementing the Fast Ray-Tracing Code to calculate self-consistent lower hybrid power deposition profiles. Heat and particle transport models that are able to reproduce the experimental JET temperature and density profiles are used in JETTO for predictive high performance modelling. Application of 3.5 MW LHCD power provides an inverted q-profile across $50-70$ % of the plasma radius whereas without LHCD, the q-profile is monotonic during the flat-top phase. The results predict that the fusion power is about 60 % higher for the high performance D-T plasmas in the optimised shear scenario with 3.5 MW LHCD applied during the high performance phase than without LHCD at $B_{\rm t} = 3.4$ T and $I_{\rm p} = 3.9$ MA on JET. Also, the width of the ITB is $0.25-0.30$ m larger and the ITB can be sustained for longer time with LHCD.

1 Introduction

Advanced steady state tokamak operation with pressure and current profile control has become now a main goal of magnetic confinement fusion research. Rapid progress in performance has been made in recent experiments with this approach. Internal Transport Barriers (ITBs) have improved the core energy confinement. Improvement of the MHD stability with reversed central magnetic shear also gives access to higher β values resulting in large bootstrap currents. Thus, moderate external current drive should be sufficient to supplement them for steady state operation. Key to sustained high performance in advanced steady state tokamak operation mode is a continuous control of pressure and current profiles.

Improved core confinement in a tokamak plasma is achieved by current profile modifications in high performance experiments [1]. The current profile can be modified with early heating by Ion Cyclotron Resonance Heating (ICRH) or Lower Hybrid Current Drive (LHCD) during the current ramp-up phase. The modified current profile together with a steep pressure gradient gives rise to reduced transport which manifests itself as a further peaking of the temperature and density profiles with steep gradients typically at $r/a = 0.5-0.7$. These internal transport barriers have a large influence on plasma core confinement and thereby significantly enhance the performance of the tokamak [2, 3, 4]. This operation mode where one of the key elements is the internal transport barrier is called the Optimised Shear (OS) scenario on JET. At present it is considered as the most promising approach towards a steady state tokamak operation.

The operation mode with internal transport barriers characteristic for the optimised shear regime combined with an edge transport barrier of the high confinement H-mode regime is called the Double Barrier (DB) mode. It has resulted in a fusion gain Q by a factor of 2 higher than in conventional sawtoothing steady state ELMy H-mode plasmas [5]. In D-T discharges the double barrier mode has produced a fusion gain of $Q = 0.4$, and high performance has been sustained for four energy confinement times in the DB mode in a D-D plasma. Recently, the double barrier mode has been routinely established in the Gas Box divertor configuration on JET.

Advanced tokamak scenario modelling with optimised magnetic shear configuration that exhibits an internal transport barrier was performed by transport simulations recently in Ref. [6]. They explored the capability of the off-axis electron cyclotron current drive to control the hollow current profile in the optimised shear operation mode. Evolution of the

thermal and the particle internal transport barriers with a monotonic or slightly reversed q-profile and large $E \times B$ rotation shear produced mainly by Neutral Beam Injection (NBI) and ICRH was studied in Ref. [7].

In this work, the performance perspectives of the profile controlled optimised shear scenario are investigated and optimised with JETTO transport code modelling calculations, using LHCD for current profile control. With LHCD, hollow current density profiles and wider reduced magnetic shear region can be achieved [1]. Thus LHCD can provide wider ITB and can stiffen its location. However, high performance OS experiments with LHCD have not been performed on JET. It is therefore important to investigate how LHCD affects the formation and sustainability of the ITB. With the direct influence on the magnetic shear and indirectly through the electron heating, LHCD can influence the transport coefficients. The lower hybrid power deposition depends sensitively on the temperature and density profiles. Accordingly, self-consistent calculation of transport and LH ray-tracing including wave absorption is required.

JETTO transport code [8] has been upgraded by adding the Fast Ray-Tracing Code (FRTC) [9] which is run inside JETTO. Lower Hybrid (LH) current density and power deposition profiles can be modelled by using either the coupled JETTO/FRTC code, the stand-alone Baranov's Ray-Tracing Code (noted in this paper as BRTC) [10] or experimental profiles of JET discharges. The self-consistent LH power deposition profiles produced by the JETTO/FRTC code can be thus compared to stand-alone ray-tracing results or to the experimental ones. In the following simulations, self-consistent current profile control with long-pulse LHCD during the high performance phase calculated by JETTO/FRTC is applied, producing significant amount of off-axis current.

The JETTO transport model is based on an empirical transport model which has been developed on JET and validated against several JET discharges [11, 12, 13]. The heat and particle transport models are further tested for optimised shear discharges with L- and ELMy H-mode plasma edge, with the main emphasis on the formation and the expansion of the internal transport barrier. The transport model in Ref. [7] differs in some detail from the model used in our transport calculations. In their study, the reproduction of the JET optimised shear pulses No. 40542 and 40847 was found to be as good as the reproduction of those two pulses with our transport model.

The paper is structured in the following way. Section 2. gives a brief characterisation and summary of the experiments in the optimised shear regime on JET. The transport model used in the transport calculations is described and tested in Sec. 3 The current profile control with LHCD is the topic of Sec. 4 The LH power deposition profiles calculated by the coupled JETTO/FRTC code are presented and compared to the profiles calculated by the stand-alone ray-tracing code. The improvements in the internal barrier formation with LHCD for OS plasmas are also discussed. The high performance steady-state discharges, including the analysis of different current ramp-up schemes, in the optimised shear scenario regime with JETTO modelling calculations are demonstrated in Sec. 5 The main plasma profiles and the parameters predicted by the modelling calculations with LHCD applied during the high performance phase are given and the MHD stability analysis is illustrated. Finally, the summary and the conclusions follow in Sec. 6

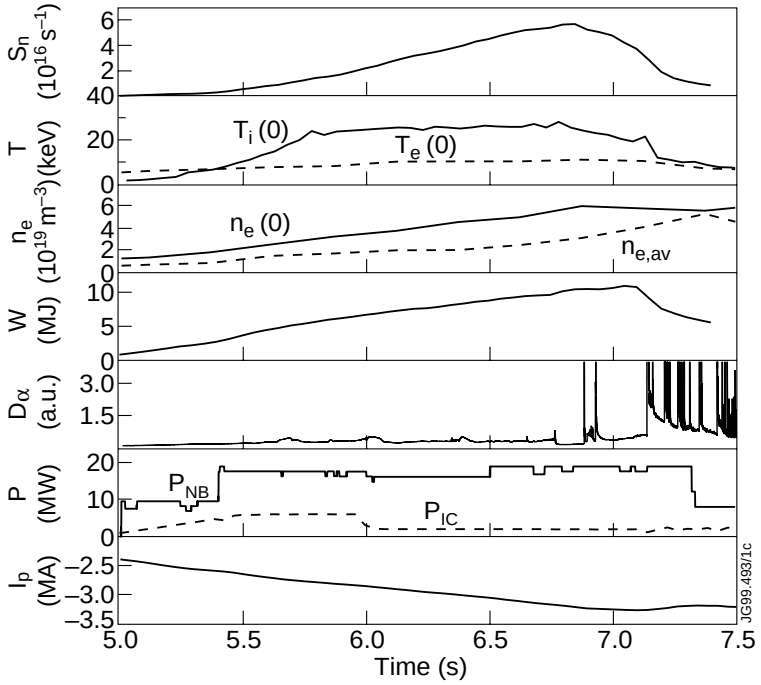

Figure 1: Time traces of the neutron rate $S_{\rm n}$, the central ion $T_{\rm i}$ and electron $T_{\rm e}$ temperatures, the electron density n_e, the diamagnetic energy W, D_α signal, the heating powers $P_{\rm NI}$ and $P_{\rm IC}$ and the plasma current $I_{\rm p}$ for the OS discharge (pulse No. 40847) with ITB and a long lasting L-mode edge. ITB appears at $t = 5.3$ s and the plasma edge experiences an L-H transition at $t = 6.76$ s.

2 Optimised Shear Experiments

The optimised shear discharge pulse No. 40847 has achieved the second highest neutron production rate in JET deuterium discharges staying only 5% below the record, also obtained with an optimised shear pulse. Pulse No. 40847 represents the standard scenario of the high performance optimised shear discharge on JET, including the typical sequence of the different confinement regimes. The characteristic time evolution of the main plasma parameters for this pulse is shown in Fig. 1.

The discharge is initiated with a fast plasma current ramp-up and an early X-point formation at $t = 0.8$ s. A short application of LHCD during the early current ramp-up phase $t = 0.4 - 1.2$ s assists to form the required target q-profile. ICRH is used for pre-heating from $t = 3 - 5$ s to slow down the current inward diffusion. High power heating with NBI and ICRH rises up to the maximum from $t = 5.0$ to $t = 5.4$ s. An internal transport barrier is formed in this pulse at $t = 5.3$ s. The peripheral plasma remains in L-mode until $t = 6.76$ s when a transition to an ELM-free H-mode occurs. The ion heat conductivity falls close to the neo-classical level in the plasma core. The region of reduced heat conductivity expands gradually with the expansion of the ITB during the L-mode phase. The ion heat conductivity is further reduced also in the peripheral region during the ELM-free H-mode phase. MHD stability is maintained near the marginal stability limit with a real time power control. At $t = 6.88$ s a first ELM marks the transition to an ELMy H-mode phase. During this last phase the performance decreases and the ITB decays.

JET pulse No. 40542 represents a shot in the double barrier mode. Internal and external

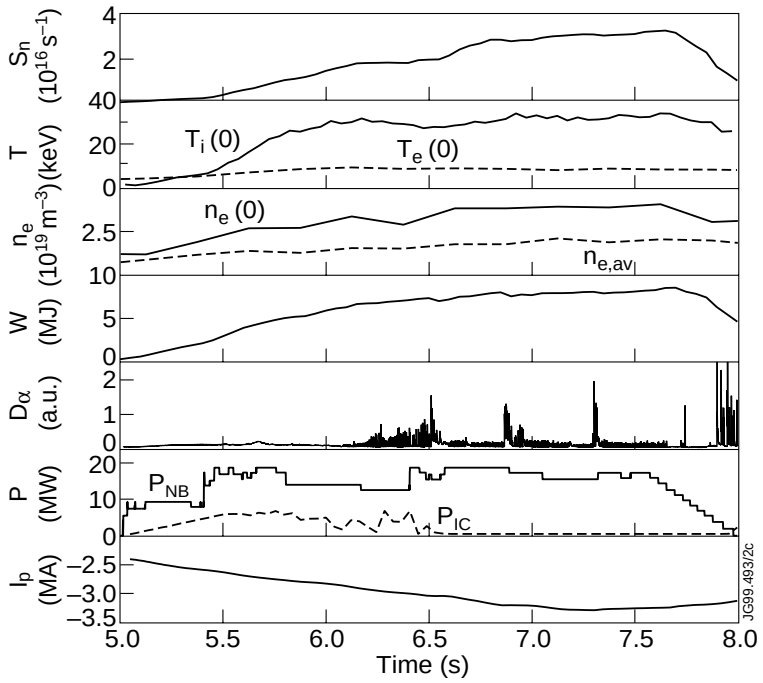

Figure 2: As in Fig. 1, but for the OS discharge (pulse No. 40542) with ITB and ELMy H-mode edge. ITB appears at $t = 5.4$ s and the plasma edge experiences an L-H transition at $t = 6.1$ s. The double barrier mode exists till $t = 7.5$ s when the heating is turned down.

transport barriers are superposed in the optimised shear scenario with the plasma edge in ELMy H-mode. The discharge approaches steady state conditions in temperature and density profiles. High performance with an H-factor $H^{89-P} \approx 2$ has been maintained for four energy confinement times. An ITB is formed in this pulse at $t = 5.4$ s. The peripheral plasma remains in L-mode until $t = 6.2$ s when a transition to an ELMy H-mode occurs. The H-mode adds an Edge Transport Barrier (ETB) to the persisting internal transport barrier. Both transport barriers co-exist for the remaining phase of high power heating until NBI power is ramped down from $t = 7.5$ s onwards. Only this ends the high performance steady state phase. The time traces for this pulse are illustrated in Fig. 2.

The ion heat conductivity χ_i falls to the neo-classical level in the plasma core. The region of reduced heat conductivity expands gradually out to 2/3 of the plasma minor radius during the L-mode phase. The extent of the improved core is maintained during the H-mode phase. The ion heat conductivity is further reduced by a factor 3 in the peripheral region during the ELMy H-mode.

The electron heat conductivity χ_e is reduced as well over the whole plasma cross section and show an ITB at the same location as seen from the ion heat conductivity profile. The reduction in the electron heat conductivity, however, is much smaller than in the ion heat conductivity. Inside the ITB, the electron heat diffusivity χ_e drops typically by a factor 5, while χ_i falls by more than an order of magnitude.

MHD stability calculations show a gradual rise of the beta limit after the pressure profile broadening with the transition to ELMy H-mode. The marginal stability limit for pressure driven kink modes then increases up to $\beta_N \approx 3$.

3 Description of the JETTO Transport Model

In this work, we will use as the basic model an empirical transport model developed at JET and tested against several different plasma discharges on DIII-D, TFTR, JT-60, ASDEX Upgrade, START and JET in L-mode and against many different plasma shots on JET in H-mode [11, 12]. It is based on a combination of a Bohm and a gyro-Bohm type of anomalous transport, and the set of transport coefficients can be written in the following form:

$$\chi_{\rm e} = 1.0\chi_{\rm gB_e} + 2.0\chi_{\rm B}, \tag{1}$$

$$\chi_{\rm i} = 0.2\chi_{\rm gB_i} + 4.0\chi_{\rm B} + \chi_{\rm i}^{\rm neo}, \tag{2}$$

$$D = [w_1 + (w_2 - w_1)\rho_{\rm eff}]\frac{\chi_{\rm e}\chi_{\rm i}}{\chi_{\rm e} + \chi_{\rm i}}, \tag{3}$$

where

$$\chi_{\rm gB_{e,i}} = 5 \times 10^{-6}\sqrt{T_{\rm e,i}}\left|\frac{\nabla T_{\rm e,i}}{B_{\rm t}^2}\right|, \tag{4}$$

$$\chi_{\rm B} = 4 \times 10^{-5} R \left|\frac{\nabla n_{\rm e} T_{\rm e}}{n_{\rm e} B_{\rm t}}\right| q^2 \times \left(\frac{T_{\rm e}(0.8\rho_{\rm max}) - T_{\rm e}(\rho_{\rm max})}{T_{\rm e}(\rho_{\rm max})}\right). \tag{5}$$

In Eqs. (4) and (5), $T_{\rm e}$ and $T_{\rm i}$ are the electron and the ion temperatures, respectively, $n_{\rm e}$ is the electron density, $B_{\rm t}$ the toroidal magnetic field, R the major radius and q is the safety factor. $\chi_{\rm i}^{\rm neo}$ is the neo-classical term for the ion heat transport. The non-locality in the Bohm transport appears in the last term where $\rho_{\rm eff}$ is the flux surface label defined by $\rho_{\rm eff} = \sqrt{\Phi/\pi B_{\rm t}}/a_{\rm eff}$ with $a_{\rm eff}$ being the radius of the circle covering the same area as the elongated plasma. $\rho_{\rm max}$ is the value of $\rho_{\rm eff}$ at the separatrix in the L-mode and on top of the barrier in the H-mode and Φ is the toroidal magnetic flux. All the quantities appearing in Eqs. (1)–(8) are expressed in SI units except the temperatures $T_{\rm e}$ and $T_{\rm i}$ whose unit is eV. w_1 and w_2, which are multipliers to the particle diffusion coefficient, are the only coefficients that are varied in the model in Eqs. (1)–(5). The boundary temperatures for the ions and electrons are taken from the experiment. Modelling of the boundary particle transport is not a well-understood problem and we have solved the problem by assuming that the recycling coefficient at the separatrix equals to one and then using the experimental particle flux through the separatrix to determine the particle losses from the plasma. The initial q-profile is calculated by EFIT and $Z_{\rm eff}$ is taken from the TRANSP analysis.

The model for triggering the internal transport barrier is introduced with a step function switching off the Bohm transport when a control parameter exceeds a certain value [13]. The suppression condition of this dimensionless control parameter and the modified Bohm transport can be thus written as

$$s - \alpha_{e,i}\Omega < 0 \tag{6}$$

$$\text{where } \Omega = \frac{\omega_{\rm E\times B}}{\gamma} \propto \frac{R\left|\frac{(RB_\theta)^2}{B}\frac{\partial}{\partial\Psi}\left[\frac{\nabla n_{\rm i} T_{\rm i}}{e n_{\rm i} R B_\theta}\right]\right|}{v_{\rm thi}} \tag{7}$$

$$\chi_{\rm B_{e,i}} = \chi_{\rm B} \times \Theta(s - \alpha_{e,i}\Omega), \tag{8}$$

where s is the magnetic shear, Ω is the ratio of shear in poloidal plasma rotation to instability growth rate, Ψ the poloidal magnetic flux, B_θ the poloidal magnetic field, e the electron charge and $\gamma = v_{\rm thi}/R$ is the characteristic growth rate of the drift type of plasma

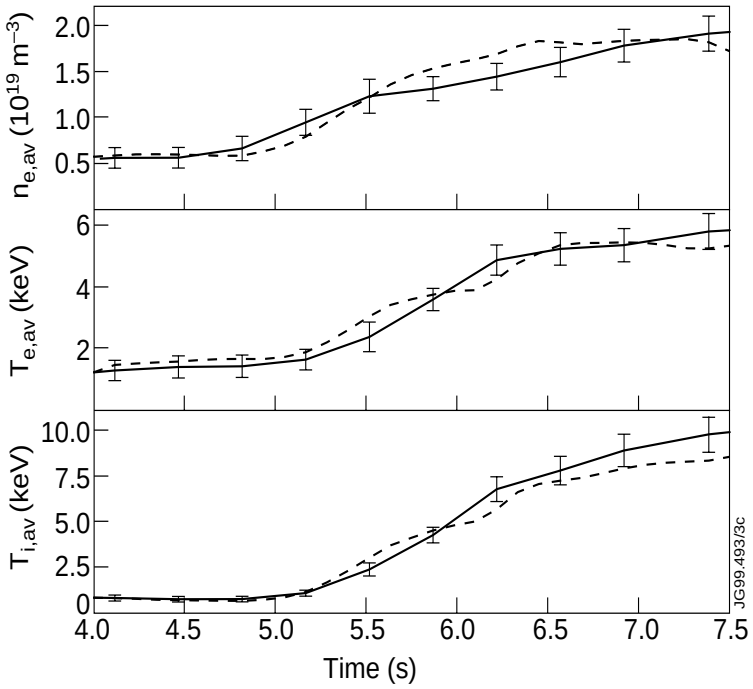

Figure 3: Reproduction of JET deuterium discharge No. 40542. Solid curve with error bars corresponds to the experiment and dashed curve is given by our transport model. The time evolution of the volume averaged electron density and the average electron and ion temperatures are shown.

turbulence and α_e and α_i are the numerical weighting factors to shear in plasma rotation Ω for the electrons and the ions, respectively. The Θ-function multiplying the modified Bohm transport in Eq. (8) is the normal Heaviside step function with the controlling parameter given by Eq. (6). The physical meaning of the step function is that in regions where the argument $s - \alpha_{e,i}\Omega < 0$, the Bohm-type of anomalous transport is fully suppressed, i.e. $\Theta = 0$, which then leads to the formation of the internal transport barrier. The contributions from the toroidal and poloidal velocities to the radial electric field and Ω are omitted in this model because of the difficulties to model the toroidal velocity and due to the lack of measurements of the poloidal rotation on JET [14]. A model which takes into account of all the three terms in the radial electric field is under construction for JETTO transport code and the first results are published in [15]. In consequence, there are four numerical parameters to be fitted with the experimental data, the coefficients α_e and α_i for triggering the ITB as well as the earlier defined w_1 and w_2 in the particle transport.

The model has been tested in the optimised shear regime against both the internal transport barrier formation in L-mode and ITB with ELMy H-mode discharges on JET. In Fig. 3, we have reproduced one steady state ITB pulse with first L-mode edge till $t = 6.2$ s and then later with ELMy H-mode edge (pulse No. 40542 that was already illustrated in Sec. 2 in Fig. 2). In particular the heat transport model can describe the temporal evolution of $T_{\mathrm{e,av}}$ and $T_{\mathrm{i,av}}$ mostly within the experimental error bars, but despite some further development of the particle transport model moderate uncertainties still persist on it. The differences in the time traces at around $t \approx 6.2$ s are related to the difficulties that the model has in following the rapid L-H transition at the plasma edge. After the delayed response to the L-H transition the transport model reproduces the experiment again nearly

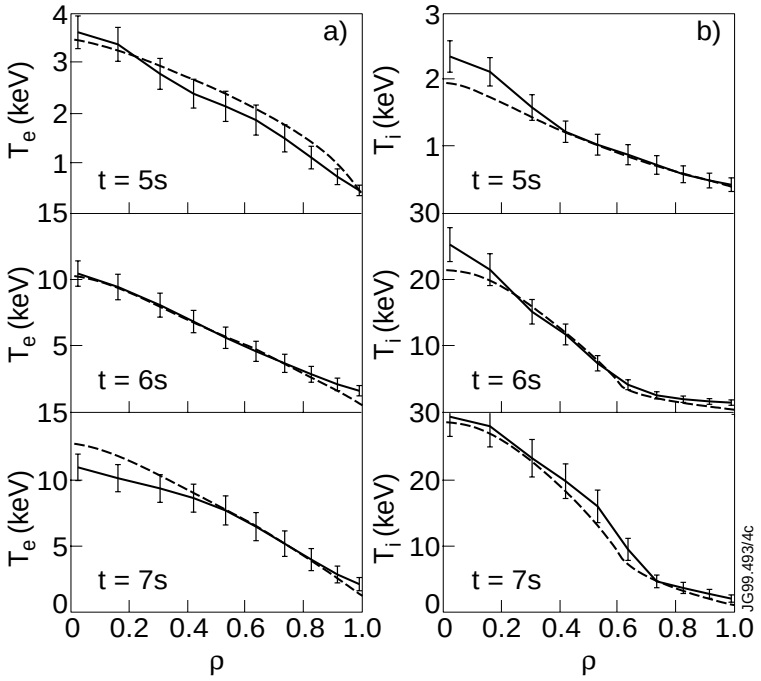

Figure 4: The radial profiles of the electron (a) and ion (b) temperatures for the reproduction of JET deuterium discharge No. 40542. Solid curve corresponds to the experiment and dashed curve is given by our transport model.

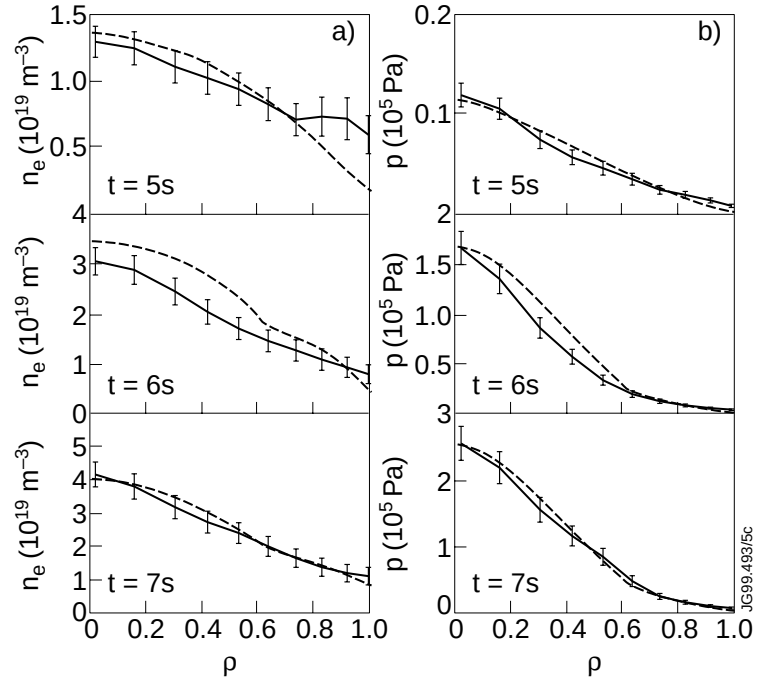

Figure 5: As in Fig. 4, but for the density (a) and pressure (b).

within the error bars after $t = 6.5$ s. In this analysis, the values $\alpha_e = 0.0$ and $\alpha_i = 1.9$ were chosen for electrons and ions, respectively, as well as $w_1 = 0.8$ (core) and $w_2 = 0.3$ (edge)

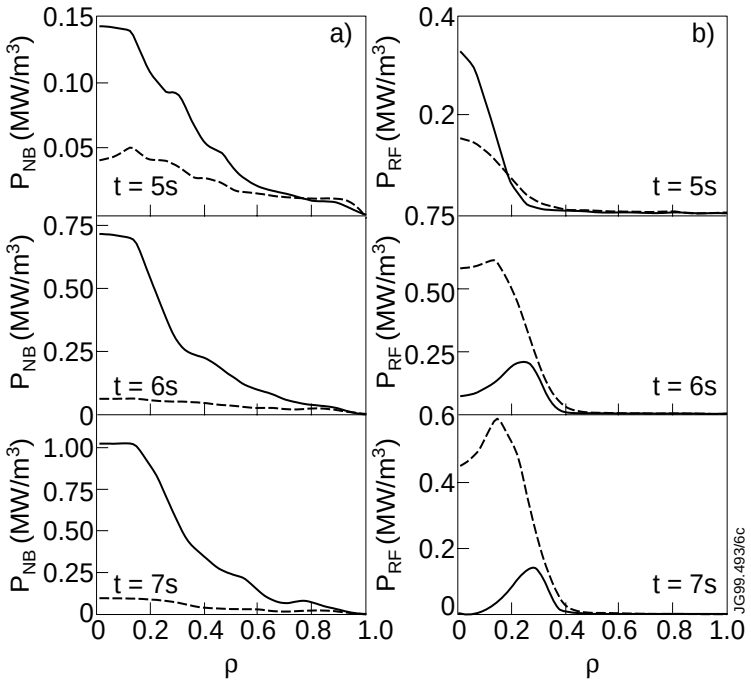

Figure 6: (a) NBI power deposition profiles and (b) ICRH power deposition profiles, both calculated by TRANSP at the same instants as the profiles in Figs. 4 and 5. The solid curves correspond to the contribution to the ion heating and dashed ones to the electron heating.

for the multipliers to the particle transport.

To quantify the agreement between the modelling and the experiments, a statistical approach to simulation results is applied according to the equations

$$m_{\mathrm{Y}} = (\sum_{i=1}^{K} \frac{\sum_{j=1}^{N} (Y_{\mathrm{exp}}(x_j) - Y(x_j))/Y(x_j)}{N})/K \tag{9}$$

$$\Delta_{\mathrm{Y}}^2 = \sum_{i=1}^{K} Z_i/K, \tag{10}$$

where Z_i is defined as

$$Z_i = \frac{\sum_{j=1}^{N} (Y_{\mathrm{exp}}(x_j) - Y(x_j) - m_{\mathrm{Y,i}})/Y(x_j)^2}{N}. \tag{11}$$

The calculated quantity m_{Y} symbolises the modelling offset of the quantity Y, which can be in our case either n_{e}, T_{e} or T_{i}, and the quantity Δ_{Y}^2 stands for the variance between the experimental measurement and the modelling result of the quantity Y. The inner summation from 1 to N is over the radial grid points ($N = 51$) and the outer summation is over 15 ($K = 15$) time points evenly distributed within the time interval of the simulation. $m_{\mathrm{Y,i}}$ is the value of m_{Y} without the sum over the time range K at the i:th time step. $Y_{\mathrm{exp}}(x_j)$ is the measured value of the given quantity at the radial point x_j and $Y(x_j)$ is the calculated one at the same point. Consequently, m_{Y} and Δ_{Y}^2 characterise the time average modelling offset and the time average modelling variance compared to the measurement over the whole duration of the simulation.

The radial profiles of the electron and ion temperatures as a function of $\rho = r/a$ at $t = 5.0$ s, $t = 6.0$ s and $t = 7.0$ s are presented in Fig. 4 (a) and (b), respectively. The central ion temperature is underestimated at $t = 5.0$ s and $t = 6.0$ s, but otherwise the profiles are in good agreement with the experiment, mostly within the error bars. In Fig. 5,

Table 1: The modelling offsets $m_{\rm te}$, $m_{\rm ti}$ and $m_{\rm ne}$ and the modelling standard deviations $\Delta_{\rm te}$, $\Delta_{\rm ti}$ and $\Delta_{\rm ne}$ for the best choice of α_i and α_e ($\alpha_i = 1.9$ and $\alpha_e = 0.0$) and the optimum case with $\alpha_i = \alpha_e$ for the pulse No. 40542.

α coefficients	$m_{\rm te}$	$m_{\rm ti}$	$m_{\rm ne}$	$\Delta_{\rm te}$	$\Delta_{\rm ti}$	$\Delta_{\rm ne}$
$\alpha_i = 1.9$, $\alpha_e = 0.0$	-0.01	0.11	0.04	0.18	0.19	0.26
$\alpha_i = 1.2$, $\alpha_e = 1.2$	0.02	0.27	0.05	0.19	0.36	0.27

the density and pressure profiles are shown at the same three instants. The modelling results are well within the error bars in H-mode, but in L-mode the model tends to overestimate the density. The calculated modelling offsets and modelling standard deviations for $T_{\rm e}$, $T_{\rm i}$ and $n_{\rm e}$ are presented in Table 1. The standard deviations for the heat transport $\Delta_{\rm te}$ and $\Delta_{\rm ti}$, calculated over the whole simulation period (from $t = 4.0$ s till $t = 7.5$ s), are clearly smaller than the standard deviation of $n_{\rm e}$ when using the model with $\alpha_i = 1.9$ and $\alpha_e = 0$. Positive modelling offsets in Table 1 indicate that those quantities are underestimated averagely over the whole time range by the transport calculation.

The power deposition profiles of NBI and ICRH are calculated by TRANSP and shown in Fig. 6 at $t = 5.0$ s, $t = 6.0$ s and $t = 7.0$ s. The maximum power for NB heating is about 18 MW and for ICRH about 7 MW. The standard Monte Carlo model was used for calculating the NB power deposition profiles. For the calculation of the ICRH power deposition profiles, the bounce-averaged Fokker-Planck code [16] was applied in TRANSP calculations. A comprehensive study of the use of that ICRH module inside TRANSP with OS plasmas and the analysis of ICRH heating for JET high performance plasmas are done in Refs. [17, 18]. The frequency of the applied ion cyclotron hydrogen minority heating scheme (minority concentration 2-3 %) was 51 MHz. The diamagnetic energy of the TRANSP analysis for this pulse is almost identical to the experimentally measured diamagnetic energy. Accordingly this can be regarded as an indirect proof of the goodness of the NBI and ICRH power deposition profiles because about 50 % of $W_{\rm dia}$ comes from the contribution of the fast particles produced by NBI and ICRH.

The time evolution of the footpoint of the internal transport barrier is shown in Fig. 7. The dashed curve corresponds to the radius of the internal transport barrier observed in the experiment (pulse No. 40542) and the solid curve is calculated by the transport model. The radial expansion of the ITB with time can be reproduced within 6 cm of the measured one by the model even if it tends to underestimate slightly the width of the barrier during the steady state phase.

The reason for fixing $\alpha_e = 0$ was that the shear in plasma rotation has only a weak or negligible effect on short wavelength turbulence which is mainly responsible for the electron heat transport. The reproduction is clearly better when $\alpha_e = 0$. The other motivated choice by the physics reasons for α_e would be $\alpha_i = \alpha_e$. In that case the optimum choice according to the modelling calculations is $\alpha_i = \alpha_e = 1.2$. However, the calculated standard deviations in Table 1 in the lower column, especially in $\Delta_{\rm ti}$, confirm the belief that $\alpha_e = 0.0$ was a justified choice.

The sensitivity analysis of the most critical numerical parameter α_i is shown in Fig. 8 where the width of the ITB is plotted as a function of α_i at $t = 7.0$ s. As can be seen, the width of the ITB decreases almost linearly with decreasing α_i and the ITB vanishes when $\alpha_i < 0.8$. The same values $w_1 = 0.8$ and $w_2 = 0.3$ were applied during the previous sensitivity analysis. The model is only weakly sensitive to the values of w_1 and w_2 according

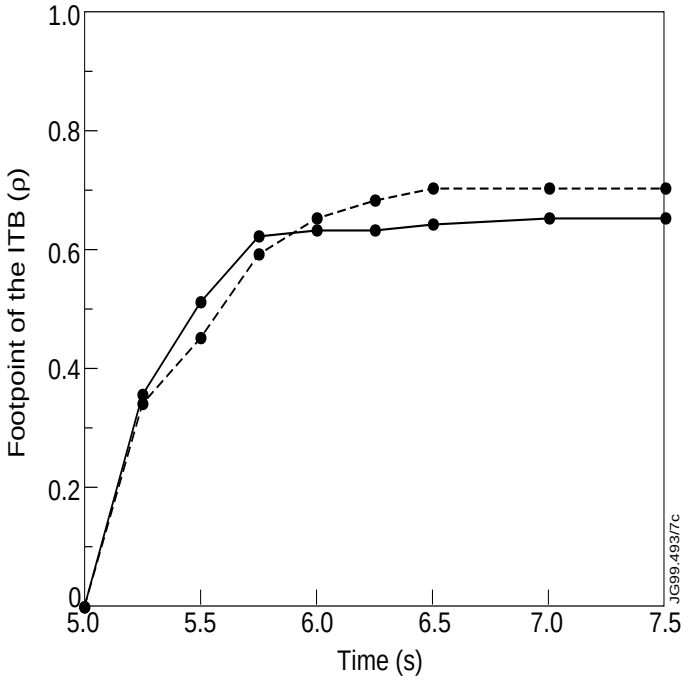

Figure 7: The radial location of the footpoint of the internal transport barrier as a function of time. Dashed curve is from the shot No. 40542 and solid curve is calculated by the transport model.

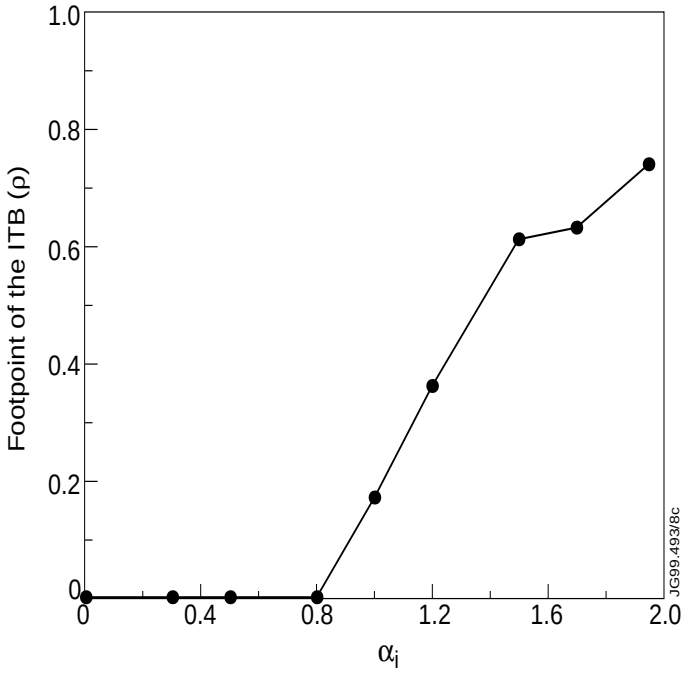

Figure 8: The radial location of the footpoint of the internal transport barrier as a function of the weighting factor α_i to shear in plasma rotation for the pulse No. 40542 at $t = 7.0$ s.

to a comprehensive sensitivity analysis in the range of $w_1 = [0.2, 2.5]$ and $w_2 = [0.2, 2.5]$.

The most critical assumption in the model is that the initial q-profile is taken from EFIT. As shown by Eq. (8), the magnetic shear s, or the q-profile has a strong effect on the ITB formation and the width of the barrier. Consequently, the accuracy of the EFIT magnetic reconstruction plays a major role in the modelling calculations. However, by starting the simulation early enough, well before the main heating phase when the current has only about $50-70$ % of its flat-top value, the current evolution calculated by JETTO should have enough time to evolve in a self-consistent way independently of the initial q-profile by EFIT. In all the previous analyses the simulations were started at least one second before the main heating phase. The optimum choice for α_i would be $10-20$ % higher (depending on the pulse) if the simulation was started at the same time as the main heating than in the case with the early start of the simulation. In the future, after validating the new Motional Stark Effect (MSE) magnetic measurements on JET, EFIT will produce more accurate q-profiles.

4 Current Profile Control and Improved ITB Formation with LHCD

Lower hybrid current drive has shown to be the most efficient of the various methods for non-inductive current drive in tokamaks so far and it has been used for current profile control in many experiments [19]. It can be applied in particular in off-axis current drive for creating or sustaining hollow current density profiles. Current profile control by LHCD has been explored and experimented by using various techniques [2, 3, 20, 21, 22]. Another means to control the current profile evolution is the current ramp-up, and its effect on optimising the fusion performance is investigated in Sec. 5.1 In this section, we concentrate on the questions of modelling of LHCD current profile for high performance optimised shear discharges and the results of modelling of the current profile control during the main heating and fuelling phase. Moreover, the improved ITB formation when applying LHCD during the main heating phase is considered.

4.1 Validation of Self-Consistently Calculated LHCD by JETTO/FRTC

A new ray-tracing code, called the Fast Ray-Tracing Code (FRTC) [9], has been installed and coupled to the JETTO transport code. The lower hybrid power deposition and current density profiles are calculated in a self-consistent way, i.e. the evolving temperature and density profiles as well as the poloidal magnetic field are read directly from JETTO by FRTC at each time step when FRTC is called. The calculated power deposition and current density profiles by FRTC are then used as the source terms for further time steps in JETTO, thus creating self-consistent transport calculation with current profile control by LHCD.

The power deposition profiles calculated by the coupled JETTO/FRTC code (solid curves) and the profiles that are calculated by the BRTC [10] (dashed curves) are compared in Fig. 9 for the pulse No. 47952. The maximum input heating powers for this recent LHCD profile control discharge are $P_{\mathrm{LH}} = 1.4$ MW and $P_{\mathrm{NB}} = 0.9$ MW, and the axial electron and ion temperatures vary between 2.0 keV and 3.5 keV as well as the axial electron density in between $1.1 - 1.7 \times 10^{19}$ m^{-3}. In each simulation, temperatures, density and I_{p} were taken from the experiment throughout the run and the only transport equation that was solved was the current diffusion equation. Power deposition profiles given by JETTO/FRTC are in a reasonably good agreement with profiles from the stand-alone BRTC as shown in

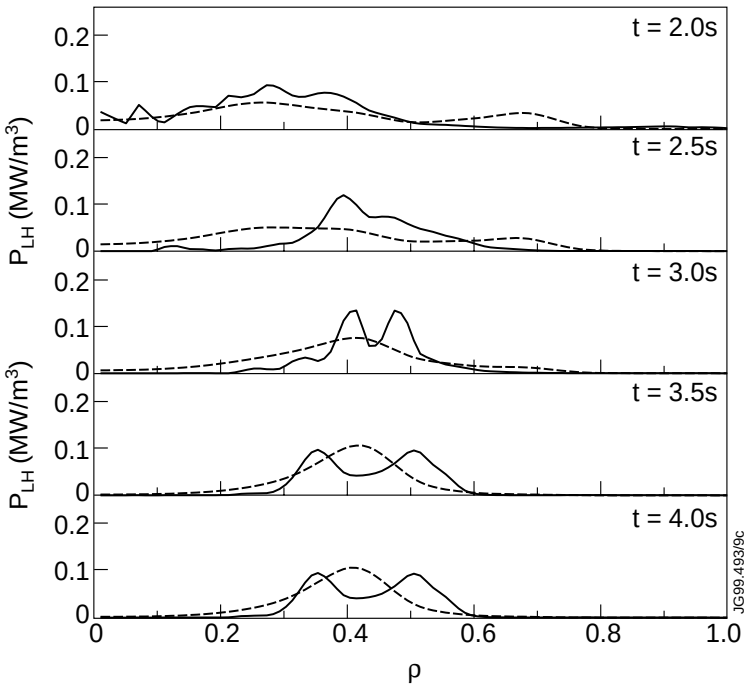

Figure 9: LH power deposition profiles calculated by the coupled JETTO/FRTC code (solid curve) and BRTC (dashed curve) for the pulse No. 47952.

Fig. 9. That argument can be also strongly motivated by following the time behaviour of the corresponding q-profiles presented in Fig. 10. The q-profile evolution is almost identical to the LH profiles by JETTO/FRTC and by BRTC, whereas without LHCD, q-profiles are completely different, i.e., they are flat or monotonic rather than strongly reversed as with LHCD. Since the q-profiles calculated by JETTO/FRTC and by BRTC are almost identical, the differences in the power deposition profiles, mostly due to stronger smoothing used in BRTC, do not affect significantly the evolution of the q-profile. However, generally it can not be concluded that the evolution of the q-profile is not sensitive to LHCD (see the dotted curves in Fig. 10). Consequently, this can be regarded as an indication of the significant agreement between the LH calculation results of FRTC and BRTC, in spite of differences in the detailed structure in LH power deposition profiles. A more comprehensive study of the properties of FRTC and its power deposition profiles has been done in Ref. [23]. Due to the lack of LHCD experiments during the high performance phase on JET, the corresponding comparison of LH profiles calculated by the two codes under those circumstances could not be accomplished.

4.2 Improved ITB Formation with LHCD

The negative or small magnetic shear s resulting from the hollow or flat current density profile is one of the two key factors suppressing the Bohm transport as can be seen in Eq. (6). However, it has not been clear how large the effect of LHCD power and the deposition profiles on the formation and location of the internal transport barrier is due to the lack of experiments where LHCD has been applied during the high performance phase on JET. Consequently, this issue was analysed by using the JETTO transport code with self-consistent LHCD deposition profiles from FRTC.

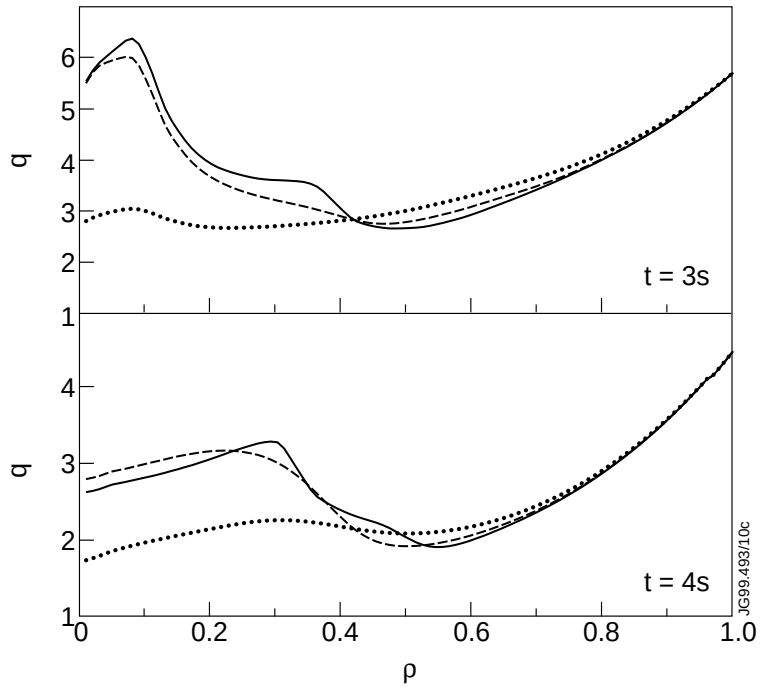

Figure 10: q-profile evolution calculated by the coupled JETTO/FRTC code (solid curve), by JETTO with LH power deposition profiles from the stand-alone BRTC (dashed curve) and without LHCD (dotted curves) for the pulse No. 47952.

Current profile control with off-axis LHCD has been applied during the high performance phase to freeze the q-profile by heating the electrons causing thus the current diffusion to slow down. Moreover, it provides additional off-axis current peaked at about $\rho = 0.6 - 0.8$ giving rise to a larger region of low magnetic shear. This dual effect of the current profile control can be seen in Fig. 11. The plasma parameters and initial temperature, density and q-profiles are from pulse No. 40542. The input heating powers and power waveform of NBI and ICRH are as shown in Fig. 6 and after that the NBI and ICRH power deposition profiles are kept fixed till $t = 10.0$ s on the level of $P_{\rm NB} = 18$ MW and $P_{\rm RF} = 6.5$ MW. The values of the numerical variables were kept as the same as in Sec. 3, i.e., $\alpha_e = 0.0$ and $\alpha_i = 1.9$ as well as $w_1 = 0.8$ and $w_2 = 0.3$.

Application of 3.5 MW LH power with power deposition and current density profiles calculated self-consistently by JETTO/FRTC provides an inverted q-profile across $50 - 70$ % of the plasma radius, whereas the q-profile is monotonic without LHCD. The reversed region in the q-profile becomes wider from the early main heating phase at $t = 6.0$ s till $t = 10.0$ s, and the changes at the plasma periphery are due to continuous current ramp-up up to $I_{\rm p} = 3.9$ MA. Thus, LHCD provides off-axis current drive in these conditions and creates a broad hollow current profile as it is seen in Fig. 11 (e). Worth mentioning here is the great significance of the amount the bootstrap current which is about 50 % of the total current. The large contribution from the bootstrap current ($\approx$ 50 %) due to the large pressure gradient over a wide region of high density in the core plasma is typical for these high performance OS plasmas according to the modelling calculations.

The radial expansion of the ITB from $\rho \approx 0.5$ to $\rho \approx 0.7$ due to LHCD is seen in Fig. 11 (c), where we have plotted the ion temperature with and without LHCD at $t =$

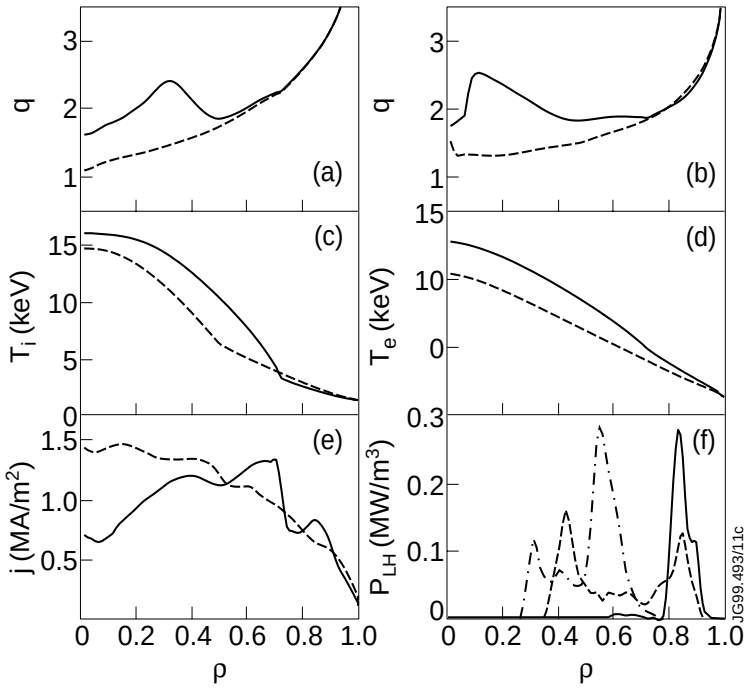

Figure 11: (a) q-profiles with 3.5 MW LHCD (solid line) and without LHCD (dashed line) at $t = 6.0$ s and (b) at $t = 10.0$ s for the high performance OS modelling discharge. (c) The ion and (d) the electron temperature as well as (e) the current density profiles with (solid) and without (dashed) LHCD at $t = 10.0$ s. (f) The LH power deposition profiles from JETTO/FRTC at $t = 6.0$ s (dash-dotted), $t = 8.0$ s (dashed) and $t = 10.0$ s (solid).

10.0 s. The electron temperature is also higher with additional 3.5 MW LHCD as shown in Fig. 11 (d). Thus the current diffusion slows down and steady state conditions with the more robust internal transport barrier can be sustained for longer time. The pressure is also higher and the region with high pressure is wider with LHCD. Both these features give rise to the better fusion performance. The pressure in our calculations is of the same order as in the record fusion discharge (DT, Hot-Ion H-mode) on JET [24]. The LH power deposition profiles calculated by JETTO/FRTC are shown in Fig. 11 (f).

The sensitivity of the formation and location of the internal transport barrier to the critical value of $\Theta(s - \alpha_{e,i}\Omega)$ used in our model for turbulence suppression were tested for the same plasma discharge (pulse No. 40542) with the same set of simulation parameters with and without off-axis current profile control by LHCD. In the model, we fixed $\alpha_e = 0.0$ as justified in Sec. 3, but α_i was varied to find out the sensitivity of the internal transport barrier formation and location to the weighting coefficient of the plasma rotation. This is shown in Fig. 12 at $t = 7.0$ s.

For lower values of α_i the stabilising effect of shear in plasma rotation on Bohm-type of transport diminishes and the transport barrier shrinks. This dependence is significantly weaker with LHCD current profile control due to the wider flat shear region. LHCD therefore not just provides wider internal transport barriers, but also stiffens the location and reduces radial fluctuations of its location due to slight variations in the shear. A similar curve was also calculated for the case with LH power of 7.0 MW, but this curve does not differ significantly from the one with 3.5 MW power. The case with $\alpha_i = 0.0$ corresponds to the

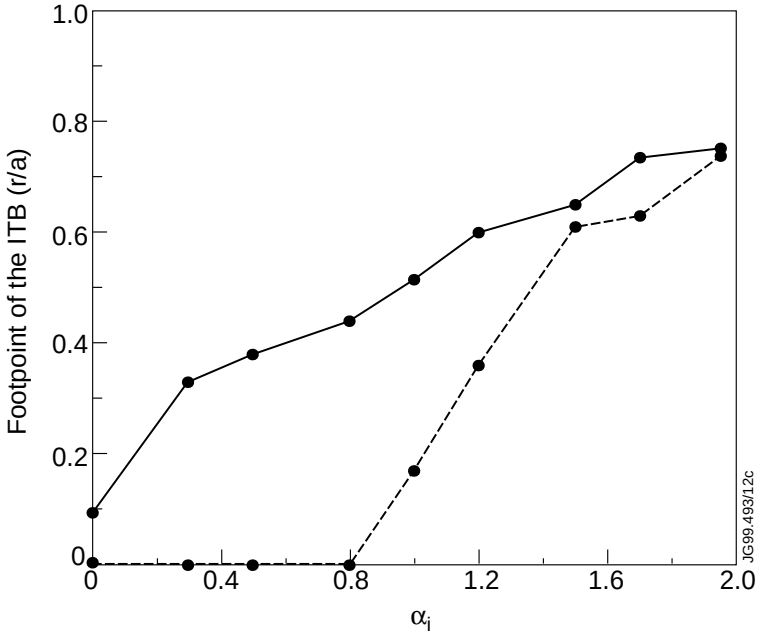

Figure 12: The radial location of the footpoint of the internal transport barrier as a function of the weighting factor α_i to shear in plasma rotation at $t = 7.0$ s. Solid curve corresponds to the case with 3.5 MW LHCD and dashed line without LHCD (pulse No. 40542).

situation where the shear in plasma rotation does not contribute to the barrier formation at all. As it is illustrated in Fig. 12, with the only contribution from the magnetic shear the transport barrier would in that case be non-existent without LHCD and very narrow (width $\approx$ 10 cm) with LHCD. However, the experimental pulse No. 40542, where no LHCD was applied to, had the internal transport barrier as shown, for example, in Fig. 4. Consequently, the contribution from the magnetic shear cannot yield the ITB alone, but the contribution from the shear in plasma rotation has to be taken into account and thus α_i must be greater than 0.

5 High Performance OS Scenarios

5.1 Effect of the Current Ramp-Up Scheme on the Current Density Profile and the ITB

Magnetic configurations which have potential for both achieving high improved confinement factor and high β_N are characterised by broad or hollow current density profiles [25]. There are several methods to create such a configuration. One of the most promising method is the lower hybrid off-axis current drive which was presented in Sec. 4 Another way to generate such a configuration is the current ramp-up.

Current ramp-up plays an important dual role because it helps to establish hollow current profile or flat q-profile in the inner half of the plasma volume, but it also helps to keep plasma not turning into an H-mode too early, presumably by keeping the H-mode threshold high through driving high edge currents. To avoid the early L-H transition is a key factor to build up high core pressure with an ITB [5]. Furthermore, the highest fusion performance

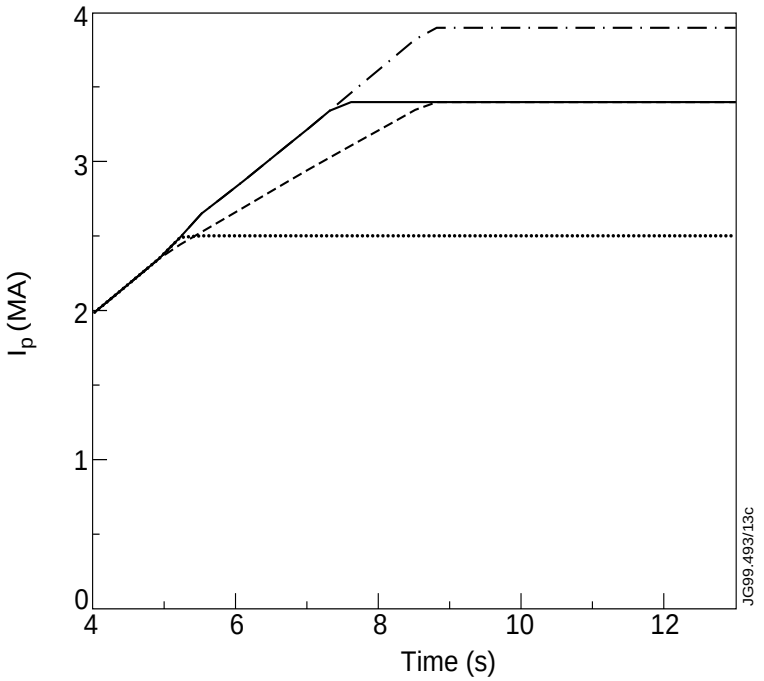

Figure 13: The four different current ramp-up schemes. The solid curve until $t = 7.5$ s corresponds to the experimental pulse No. 40542. The curves correspond to the following current ramp-up schemes: fast ramp-up speed ($dI_p/dt = 0.4$ MA/s) with flat-top value of $I_p = 3.9$ MA (dash-dotted curve), fast ramp-up with $I_p = 3.4$ MA (solid curve), slow ramp-up ($dI_p/dt = 0.28$ MA/s) with $I_p = 3.4$ MA (dashed curve) and $I_p = 2.5$ MA (dotted curve).

in D-D plasmas on JET has been obtained when an H-mode transition was delayed as long as possible [1, 24].

We have analysed in a predictive way four different current ramp-up schemes with the JETTO transport code. Either the total plasma current or the current ramp-up speed is varied, but the other plasma and simulation parameters (except the toroidal magnetic field B_t that is varied in accordance with the steady state level of I_p) are kept fixed. The four different current ramp-up schemes used in this current ramp-up modelling of JET optimised shear plasmas are presented in Fig. 13.

The current density, the magnetic shear s and the ion temperature profiles for these simulations are shown in Fig. 14 at $t = 10.0$ s when the plasma reaches the steady state level of the plasma current. The initial temperatures, density and q-profile at $t = 4.0$ s were taken from the pulse No. 40542. The current profiles are almost similar to each other in the core region. However, at radii larger than $\rho \approx 0.5$ they are strongly modified. The centre of the plasma is not affected due to the high electron temperature which effectively prevents the current diffusion, whereas in the plasma periphery, the larger the plasma current, the more hollow is the current profile and correspondingly, the smaller is the magnetic shear. What is also interesting is that the faster current ramp-up (solid curve) with equal flat-top value of the current gives a more hollow current profile and thus smaller magnetic shear than the slower current ramp-up speed (dashed curve). This gives rise to higher temperature, larger pressure and thus larger fusion power.

The simple conclusion when comparing the different current ramp-up schemes is that

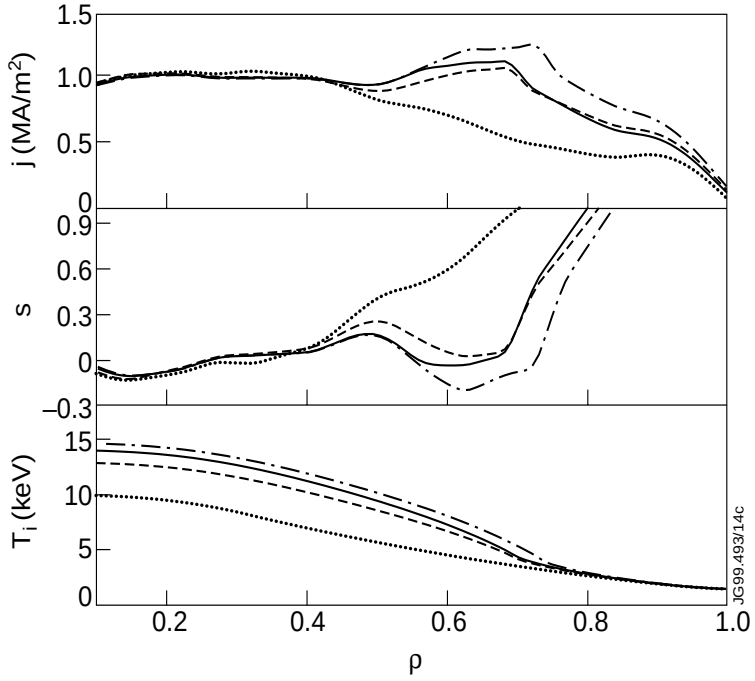

Figure 14: Current density j, magnetic shear s and ion temperature profiles T_i for the four current ramp-up schemes as presented in Fig. 13 with the same notations of the curves at $t = 10.0$ s.

with higher q_a (smaller I_p) shrinking of the internal transport barrier is caused by the higher edge shear. Accordingly, the region of low shear increases in size with lower q_a. This can be seen in Fig. 14 where the internal transport barrier in the ion temperature is at about $\rho = 0.35$ with $I_\mathrm{p} = 2.5$ MA and at about $\rho = 0.73$ with $I_\mathrm{p} = 3.9$ MA. Consequently, the best fusion performance for OS plasmas is expected to be obtained with the highest current and with the fastest stable current ramp-up speed which was also confirmed on JET during DTE1 [26].

5.2 Fusion Performance Achieved with combined LHCD and Fast Current Ramp-Up

The starting point for the analysis of the high performance discharges with modelling calculations is the reproduction of the pulse No. 40542, but the calculation is extended by 5 s beyond the real JET discharge. Consequently, the main heating phase lasts more than 5 s longer than the experiment and the plasma reaches steady state after $t = 10$ s. The reason for choosing this pulse as the initial and the main heating and fuelling phase till $t = 7.5$ s is that it has suitable steady state like features and benign properties against MHD instabilities. Due to the uncertainties persisting on the particle transport model, the multipliers w_1 and w_2 to the particle diffusion coefficient are varied and the differences in the performance predictions are illustrated. After a comprehensive sensitivity analysis of w_1 and w_2 in the range of $w_1 = [0.2, 2.5]$ and $w_2 = [0.2, 2.5]$ we show two different sets of w_1 and w_2 with the first set being $w_1 = 0.8$ and $w_2 = 0.3$ (set 1) and the second one $w_1 = 1.6$ and $w_2 = 0.6$ (set 2). Set 1 corresponds to the same values as used in Sec. 3 and set 2 represents a more conservative choice of w_1 and w_2 in the transport calculation. The plasma current is as

for the pulse No. 40542 till $t = 7.5$ s and afterwards it is as optimised in Sec. 5.1, i.e., the flat-top plasma current is 3.9 MA with fast current ramp-up speed, and the toroidal magnetic field is 3.4 T. The heating power and the deposition profiles of NBI and ICRH are kept fixed since the last experimental deposition profiles calculated by TRANSP. NBI power deposition profiles did not change significantly according to PENCIL calculations although density would be more than two times larger at $t = 10.0$ s. The LH power deposition profiles used in the analysis are calculated self-consistently by JETTO/FRTC.

The experimental pressure profile is better reproduced with the model with a lower particle diffusion multiplier (set 1) at $t = 7.0$ s as shown in Fig. 15 (a). The radial location of the internal transport barrier ($\rho \approx 0.7$) is well reproduced by the model with smaller w_1 and w_2 whereas the model with larger w_1 and w_2 underestimates the width of the barrier. The pressure is slightly overestimated by the model with set 1 and strongly underestimated by the model with set 2. The time traces of the average electron density and the average electron and ion temperatures are illustrated in Fig. 15 (b). The average density yielded by the model with set 1 is about 50 % higher than in the model with set 2, partly due to smaller w_1 and w_2, but mostly due to the smaller particle flux out of the plasma in the model with set 1. The differences in temperatures are much smaller between the models, but due to the applied LHCD power of 3.5 MW, the electron temperature in the simulated discharges is significantly higher especially at the beginning of the discharge. The experimental ion temperature is higher at $t \approx 7.5$ s, presumably for two different reasons. Firstly, because in the experiment NBI was turned down, but ICRH was turned up again towards $t = 8$ s whereas in the modelling calculations the powers of NBI and ICRH are on the same level as at $t = 6$ s and secondly, due to the tendency for the model to underestimate slightly the ion temperature as shown already in Figs. 3 and 4.

The evolution of the radial profiles is illustrated in Fig. 16. The ion temperature rises rapidly in the beginning during the low density phase, but due to the continuous density rise with beam fuelling it starts to decrease after $t = 7.0$ s. The electron temperature remains fairly constant after $t = 6.0$ s whereas the density rises till $t = 10.0$ s where the steady state is reached. The expansion of the internal transport barrier occurs mostly between $t = 5.3$ s and $t = 6.0$ s. One reason for the expansion of the ITB with time is the broadening of the low magnetic shear region as shown in Fig. 16 (d) which can be explained by the applied $P_{\mathrm{LH}} = 3.5$ MW LHCD and the continuous current ramp-up till $t = 9.5$ s. The magnetic shear is negative inside about $50 - 70$ % of the plasma radius. q_{95} is between 3 and 4 and settles during the steady state phase down to 3.1. Worth noticing is also the large contribution (≈ 50 %) from the bootstrap current which is produced in the large pressure gradient region, i.e. in the same region where the footpoint of the ITB is located, thus giving rise to larger current and smaller magnetic shear in that region.

The time evolution of the fusion power is shown in Fig. 17 (a) (upper half) for the range between the two different sets (set 1 and set 2) of multipliers w_1 and w_2. Fusion power in the range 20-30 MW is predicted for $I_{\mathrm{p}} = 3.9$ MA, $B_{\mathrm{t}} = 3.4$ T discharges. Flat-top conditions are obtained at $t \approx 10$ s, after about 5 s from the start of the main heating phase with input heating powers of $P_{\mathrm{NB}} = 18$ MW, $P_{\mathrm{RF}} = 6.5$ MW (composed of 2/3 on-axis and 1/3 off-axis deposition) and $P_{\mathrm{LH}} = 3.5$ MW as illustrated in Fig. 17 (a) (bottom).

The same two simulations (set 1 and set 2) as shown in Figs. 15 and 17 were also performed without LHCD. In each run, ITB was formed slightly later and its width stayed about 10 cm narrower till $t = 7.0$ s than in the simulation with LHCD. After $t = 7.0$ s ITB started to shrink and finally at $t \approx 8$ s, the width of the ITB settled down to $\rho \approx 0.4$. The fusion power was only about $50 - 60$ % of the fusion power with LHCD and the average ion

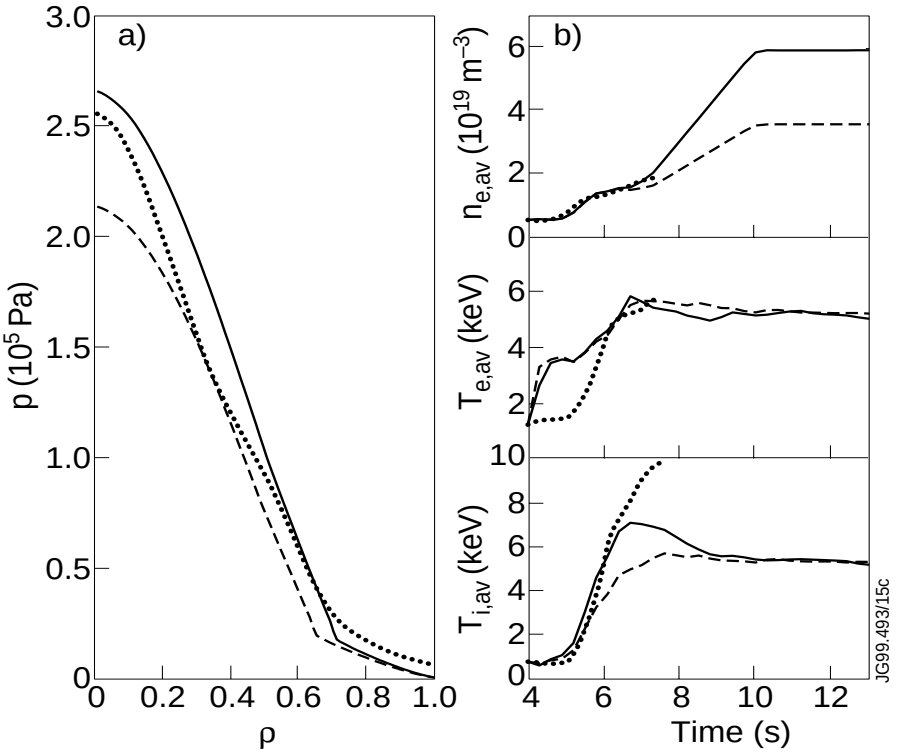

Figure 15: (a) The experimental (dotted, pulse No. 40542) and two simulated pressure profiles with lower (solid) and higher (dashed) particle diffusion multipliers w_1 and w_2 at $t = 7.0$ s. (b) The average electron density and the average electron and ion temperatures with the same markings as a function of time.

temperature about 80 %.

The predicted fusion power in fact exceeds clearly the total external input power over the whole plasma core region as shown in Fig. 17 (b). The case with the larger fusion power (set 1) is stable against MHD instabilities with a beta value $\beta_N \approx 2.4$ as is seen as a point on the $\beta_N \approx 2.4$ curve in Fig. 17 (c) and has a limit of $\beta_N \approx 3$, including the wall stabilisation with the wall at $r/a = 1.3$ compatible with previous JET results. The most limiting instability is the pressure driven global $n = 1$ kink instability which is a typical limiting factor for the high performance optimised shear discharges in the double barrier mode on JET [27]. However, this MHD stability analysis does not concern tearing modes nor $q = 2$ snakes which limit the high performance of JET OS plasmas.

Recent experiments on JET have shown that in the double barrier mode density does not increase with time in the way as predicted by our transport model. In experiments density typically saturates at the level of $4 - 5 \times 10^{19}$ m^{-3} whereas the ion temperature continues to rise up to 40 keV. However, ion temperatures saturated at the level of 15-20 keV with continuous density rise would be more desirable for reaching the highest fusion performance. The best OS discharges on JET maintain quasi steady state conditions for up to 3 energy confinement times with neutron yields up to equivalent $Q_{DT} \approx 0.4$ at typical $\beta_N \approx 2$ [28]. The effect of the experimentally observed density saturation was not taken into account in our modelling calculations and as a result, we may overestimate the fusion performance. With an L-mode plasma edge experiments, density is not saturated, but their problem are

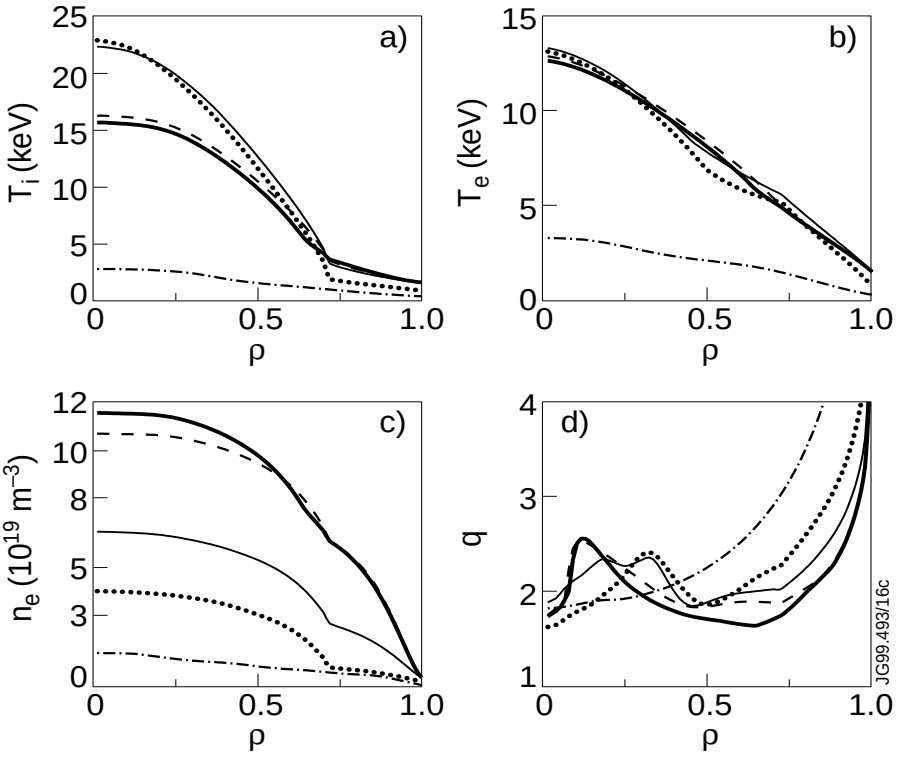

Figure 16: The radial profiles of (a) ion temperature, (b) electron temperature, (c) electron density and (d) q-profile at $t = 4.0$ s (dash-dotted curve), $t = 6.0$ s (dotted curve), $t = 8.0$ s (solid curve), $t = 10.0$ s (dashed curve) and $t = 13.0$ s (thick solid curve).

the disruptions caused by the pressure driven kink modes [5].

6 Summary and Conclusions

Lower hybrid current drive control with transport calculations has been investigated with JETTO transport code. JETTO has been upgraded by implementing the FRTC code that calculates, coupled with JETTO, LH power deposition and current density profiles. The heat transport model has been further tested in L-mode and ELMy H-mode with ITB, and various particle transport models have been used in JETTO to model predictive high performance discharges in the optimised shear double barrier operation mode. The JETTO transport model has been able to reproduce the formation and evolution of the internal transport barriers in fair agreement, mostly within the experimental error bars, with experiments.

The LH power deposition profiles calculated by JETTO/FRTC are in good agreement with the profiles calculated by BRTC. Evolution of the q-profile does not seem to depend on whether the LH power deposition and current density profiles are taken from FRTC or BRTC.

Improved internal transport barrier formation with off-axis lower hybrid current drive calculated by JETTO/FRTC was found in transport calculations. LHCD provided wider ITBs and stiffened their location by reducing the magnetic shear in the OS regime. Current density profiles were hollow and wider regions with reduced transport due to the negative magnetic shear as well as steady state conditions with more robust ITBs could be sustained for longer time. Without LHCD, q-profiles were monotonic, whereas application of 3.5 MW

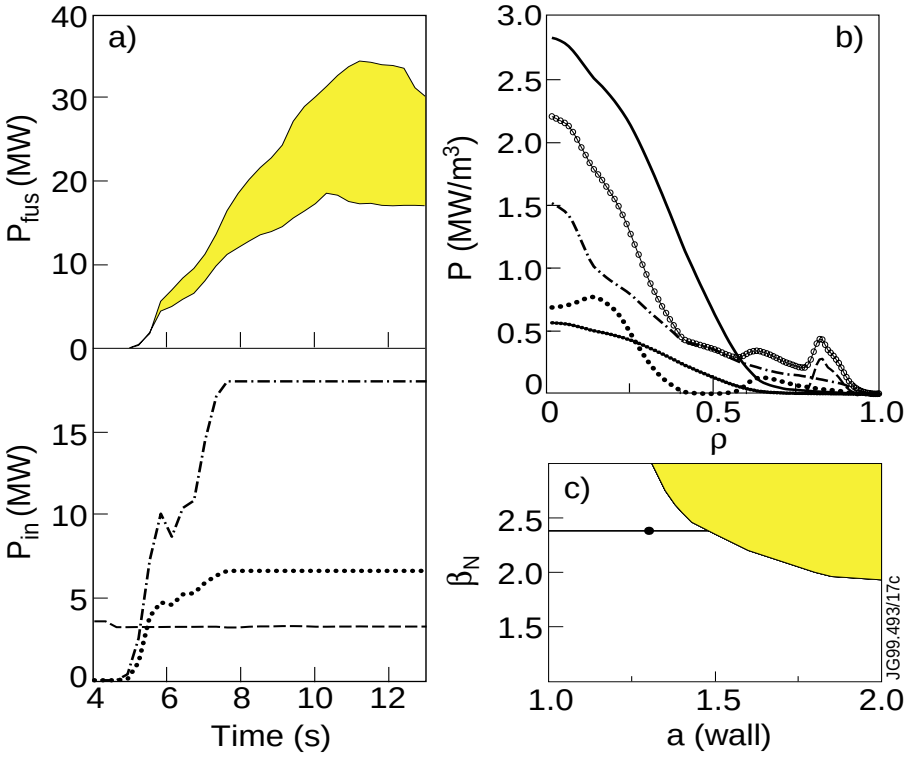

Figure 17: (a) Time evolution of the fusion power calculated by the two different transport models and the input powers (NB=dash-dotted, RF=dotted, LH=dashed). (b) The radial profiles of the input heating powers (NB=dash-dotted, RF=dotted, LH=dashed, NB+RF+LH=solid curve with circles) and produced fusion (solid curve) and alpha heating powers (thick solid curve) with the transport model of the smaller particle diffusion coefficient (set 1) at $t = 13.0$ s. (d) MHD stability analysis of the scenario with the largest fusion power at $t = 13.0$ s. The shaded area is unstable with $n = 1$ kink instability as the limiting factor.

LH power provided inverted q-profiles across $50 - 70$ % of the plasma radius.

Four different current ramp-up schemes were analysed with JETTO. The total plasma current or the current ramp-up speed were varied keeping the other plasma parameters fixed. In the core region the current density profiles were not affected, but at larger radii they were strongly modified. ITBs were wider with larger currents and faster current ramp-up speeds. In conclusion, shrinking of the ITBs are caused by higher edge shear, i.e. higher q_a (smaller I_p). Consequently, the best fusion performance for OS plasmas is expected to obtain with the highest current and the fastest stable current ramp-up speed.

The transport modelling results of the high performance JET plasma in the optimised shear regime in the double barrier mode at $I_p = 3.9$ MA and $B_t = 3.4$ T predicted a fusion power in the range of 20-30 MW with $Q \approx 0.7 - 1$. Application of 3.5 MW LHCD was crucial in order to achieve the high performance because without LHCD the fusion power was only about $50 - 60$ % of the fusion power with LHCD and the ITB shrank from $\rho \approx 0.7$ to $\rho \approx 0.4$ when LHCD was not applied. Considerable uncertainties still exist, in particular, in the JET particle transport model. The peak performance was analysed to be stable against the kink and ballooning instabilities. However, even if the usually dominating $n = 1$ kink mode was stabilised, the MHD stability analysis did not include neoclassical tearing modes

nor $q = 2$ snakes which can affect considerably the transport and lead to a soft roll-over and thus limit the performance and the duration of the high performance phase of the OS discharge.

One of the key elements during the high performance phase is the increase and the evolution of the density [29]. Steady state conditions were achieved only 5 s after the beginning of the main heating and fuelling phase at $t \approx 10$ s. The limiting factor was the slow fuelling rate from NBI. Higher fuelling rates by additional gas puffing or pellet injection than available from NBI alone would be necessary to raise the core density and the global performance faster [30]. However, until now no ITB with additional gas puffing or pellet injection can be formed or sustained on JET and thus they were not included in the modelling calculations for improving the performance. The recently installed high field side pellet launcher on JET can provide a route to increase density with pellet fuelling without losing ITB.

In addition to the fuelling problem, the high performance DT optimised shear discharges on JET tokamak during DTE1 campaign were limited to less than five seconds duration due to technical restrictions on the high power heating systems and the neutron budget. However, in the light of our modelling results there is a reason to suppose that the high current DT optimised shear pulses could be extended to truly steady state operation with no destruction of the ITB and no significant loss of performance. The key element is the efficient current profile control by LHCD during the high performance phase.

Acknowledgements

The authors are grateful to Dr. Guido Huysmans for providing them with the MHD stability calculations. The authors also thank Prof. Alexiy Piliya and Dr. Alexander Saveliev for implementing the FRTC ray-tracing code into JETTO. The NB power deposition profile calculations with PENCIL by Dr. Andrew Bickley are also highly appreciated. Special thanks also belong to Dr. David Heading and Dr. Gerard Corrigan for technical assistance.

References

[1] THE JET TEAM (presented by F.X. Söldner), Plasma Phys. Control. Fusion **39** (1997) B353.

[2] LEVINTON, F.M., et al., Phys. Rev. Lett. **75** (1995) 4417.

[3] STRAIT, E.J., et al., Phys. Rev. Lett. **75** (1995) 4421.

[4] GORMEZANO, C., THE JET TEAM, ibid., p. 487.

[5] SÖLDNER, F.X., et al., Nucl. Fusion **39** (1999) 407.

[6] MURAKAMI, M., et al., Proc. of the 26th European Physical Society Conference on Controlled Fusion and Plasma Physics, Maastricht, the Netherlands, 14-18 June, ECA **23J** (1999) 1213.

[7] VOITSEKHOVITCH, I., et al., Proc. of the 26th European Physical Society Conference on Controlled Fusion and Plasma Physics, Maastricht, the Netherlands, 14-18 June, ECA **23J** (1999) 957.

[8] GENACCHI, G., TARONI, A., JETTO: A Free Boundary Plasma Transport Code (Basic Version), Rapporto ENEA RT/TIB 1988(5).

[9] ESTERKIN, A.R., PILIYA, A.D., Nucl. Fusion **36** (1996) 1501.

[10] BARANOV, Yu.F., et al., Nucl. Fusion **36** (1996) 1031.

[11] ERBA, M., et al., Plasma Phys. Control. Fusion **39** (1997) 261.

[12] ERBA, M., et al., Validation of a New Mixed Bohm/gyro-Bohm Transport Model on Discharges of the ITER Data-Base, JET Report JET-R(96)07 (1996).

[13] PARAIL, V.V., et al., Nucl. Fusion **39** (1999) 429.

[14] BARANOV, Yu.F., et al., Nucl. Fusion **39** (1999) 1463.

[15] PARAIL, V.V., et al., Proc. of the 26th European Physical Society Conference on Controlled Fusion and Plasma Physics, Maastricht, the Netherlands, 14-18 June, **23J** (1999) 181.

[16] SMITHE, D.N., et al., Proceedings of the 8th Topical Conference on Radio-Frequency Power in Plasmas (AIP, New York) (1989) 338.

[17] COTTRELL, G.A., et al., Nucl. Fusion **39** (1999) 389.

[18] MANTSINEN, M.J, et al., Plasma Phys. Control. Fusion **41** (1999) 843.

[19] EKEDAHL, A., et al., Nucl. Fusion **38** (1998) 1397.

[20] HUGON, M., et al., Nucl. Fusion **32** (1992) 33.

[21] MOREAU, D., et al., Plasma Phys. and Control. Nucl. Fusion Research (Proc. of the 14th Int. Conf. Würzburg 1992) Vol. 1 (Vienna : IAEA) 921.

[22] GORMEZANO, C., et al., Applications of Radiofrequency Power to Plasmas (Proc. of the 12th Top. Conf. Savannah Georgia 1997) (New York : American Institute of Physics) 3.

[23] HEIKKINEN, J.A., et al., Plasma Phys. Control. Fusion **41** (1999) 1231.

[24] KEILHACKER, M., et al., Nucl. Fusion **39** (1999) 209.

[25] LITAUDON, X., Plasma Phys. Control. Fusion **40** (1998) A251.

[26] HORTON, L.D., et al., Nucl. Fusion **39** (1999) 993.

[27] HUYSMANS, G.T.A., et al., Proc. of the 24th European Physical Society Conference on Controlled Fusion and Plasma Physics, Berctesgaden, Germany, **21A(1)** (1997) 21.

[28] ZASTROW, K.-D., et al., Proc. of the 26th European Physical Society Conference on Controlled Fusion and Plasma Physics, Maastricht, the Netherlands, 14-18 June, **23J** (1999) 217.

[29] SIPS, A.C.C., et al., Plasma Phys. Control. Fusion **40** (1998) 1171.

[30] SÖLDNER, F.X., et al., Proc. of the 26th European Physical Society Conference on Controlled Fusion and Plasma Physics, Maastricht, the Netherlands, 14-18 June, **23J** (1999) 185.